Ensemble cryo-electron microscopy reveals conformational states of the nsp13 helicase in the SARS-CoV-2 helicase replication-transcription complex

James Chen[1,6], Qi Wang[2,6], Brandon Malone[1,6], Eliza Llewellyn[1], Yakov Pechersky[2], Kashyap Maruthi[3], Ed T. Eng[3], Jason K. Perry[4], Elizabeth A. Campbell[1], David E. Shaw[2,5,7], Seth A. Darst[1,7,8]

[1]Laboratory of Molecular Biophysics, The Rockefeller University, New York, NY 10065 USA.

[2]D. E. Shaw Research, New York, NY 10036 USA.

[3]The National Resource for Automated Molecular Microscopy, Simons Electron Microscopy Center, New York Structural Biology Center, New York, NY 10027 USA.

[4]Gilead Sciences, Inc., Foster City, CA 94404 USA.

[5]Department of Biochemistry and Molecular Biophysics, Columbia University, New York, NY 10032 USA.

The authors declare no conflict of interest

[6]These authors contributed equally to this work.

[7]Correspondence to: David.Shaw@DEShawResearch.com; darst@rockefeller.edu

[8]Lead contact: darst@rockefeller.edu

The SARS-CoV-2 nonstructural proteins coordinate genome replication and gene expression. Structural analyses revealed the basis for coupling of the essential nsp13 helicase with the RNA dependent RNA polymerase (RdRp) where the holo-RdRp and RNA substrate (the replication-transcription complex, or RTC) associated with two copies of nsp13 (nsp13$_2$-RTC). One copy of nsp13 interacts with the template RNA in an opposing polarity to the RdRp and is envisaged to drive the RdRp backwards on the RNA template (backtracking), prompting questions as to how the RdRp can efficiently synthesize RNA in the presence of nsp13. Here, we use cryo-electron microscopy and molecular dynamics simulations to analyze the nsp13$_2$-RTC, revealing four distinct conformational states of the helicases. The results suggest a mechanism for the nsp13$_2$-RTC to turn backtracking on and off, using an allosteric mechanism to switch between RNA synthesis or backtracking in response to stimuli at the RdRp active site.

COVID-19, caused by the coronavirus SARS-CoV-2 [1,2], continues to devastate the world. The viral RNA-dependent RNA polymerase (RdRp, encoded by non-structural protein 12, or nsp12) functions as a holo-RdRp (comprising nsp7/nsp8$_2$/nsp12) in a replication-transcription complex (holo-RdRp + RNA, or RTC) to direct RNA synthesis from the viral RNA genome [3–5]. The RdRp is also a target for the clinically approved antiviral remdesivir [6–8]. In addition to the holo-RdRp, the virus encodes several nucleic acid processing enzymes, including a helicase (nsp13), an exonuclease (nsp14), an endonuclease (nsp15), and methyltransferases (nsp14 and nsp16) [9]. Little is known about how these enzymes coordinate to replicate and transcribe the viral genome.

Nsp13, essential for viral replication [10–13], is a superfamily 1B (SF1B) helicase that can unwind DNA or RNA substrates with a 5'->3' directionality [14–16]. Along with the two canonical RecA ATPase domains of SF1 helicases [14,17], nsp13 contains three additional domains; an N-terminal zinc-binding domain (ZBD, unique to nidoviral helicases), a stalk, and a 1B domain [13,18,19]. Prior studies established that the nsp13 helicase forms a stable complex with the RTC, and single-particle cryo-electron microscopy (cryo-EM) structures of an nsp13$_2$-RTC (the RTC with two nsp13 protomers bound) have been determined [20–22].

In the nsp13$_2$-RTC structure, two protomers of nsp13 (nsp13.1 and nsp13.2; Fig. 1) sit on top of the RTC with each nsp13-ZBD interacting with one of the two N-terminal helical extensions of nsp8 [20–22]. This overall architecture places the nsp13.1 active site directly in the path of the downstream template-RNA (t-RNA). The cryo-EM maps showed that the 5'-single-stranded overhang of the t-RNA (Fig. S1) passed through the nucleic acid binding channel of nsp13.1 [23], but the low resolution of the map due to structural heterogeneity precluded detailed modeling [20].

The structural analysis of the nsp13$_2$-RTC provided new perspectives into the role of the nsp13 helicase in the complex viral replication-transcription program, suggesting that nsp13 may facilitate processive elongation by the RdRp on the highly structured RNA genome [24,25], but may also generate backtracked RTCs for proofreading, template-switching during sub-genomic RNA transcription, or both [20,26]. How nsp13 directs these diverse processes that regulate RdRp function remains less

understood. For instance, the structures indicate that nsp13 translocates on the t-RNA strand in the 5'->3' direction [16], while the RdRp would translocate on the same strand in the opposite direction (Fig. 1B). How can the RdRp rapidly replicate the ~30 kb viral genome [27] if it is opposed by the helicase? Also, what is the role of the second nsp13 protomer (nsp13.2), which appears capable of ATPase and translocation/helicase activity but does not appear to be engaged with nucleic acid in the structures [20,26]?

Here we describe an extensive structural analysis of a cryo-EM dataset of the nsp13-RTC, combined with molecular dynamics (MD) simulation analysis of the resulting structures. The results yield a cryo-EM map of the $nsp13_2$-RTC at a nominal resolution of 2.8 Å (2.1-2.5 Å in the active site core of the RdRp; Fig. 1). Structural heterogeneity apparent in the nsp13 portions of the map was resolved by classification approaches, revealing four distinct conformational states of the nsp13 subunits. Analysis of these conformational states suggest solutions to the apparent contradictions regarding the role of nsp13 and provides further insight into models for nsp13 function during viral replication/transcription.

RESULTS

An augmented cryo-EM dataset allows extensive structural analysis of the nsp13-RTC. Previously we described a single-particle cryo-EM analysis of a stable SARS-CoV-2 nsp13-RTC from a curated set of 88,058 particle images [20]. These particles were classified into three distinct assemblies, $nsp13_1$-RTC (4.0 Å nominal resolution), $nsp13_2$-RTC (3.5 Å), and a dimer of $nsp13_2$-RTC [$(nsp13_2\text{-RTC})_2$; 7.9 Å]. Here we analyzed a much larger dataset (nearly five times as many particles; Fig. S1, Table S1) collected from the same sample preparation. From a consensus refinement (Figs. S1 and S2, map1; Note: Fig. S1 shows the details of the cryo-EM processing pipeline; Fig. S2 is a streamlined cryo-EM processing pipeline that highlights the essential steps), the particles were classified [28] into the same three assemblies observed previously [$nsp13_1$-RTC (map2), $nsp13_2$-RTC (map3), $(nsp13_2\text{-RTC})_2$ (map4)] [20] with a very similar distribution of particles between the three assemblies (Figs. S1 and S2; Tables S1 and S2), confirming the robustness of the classification procedure. We focus primarily on the $nsp13_2$-RTC because the bulk of the particles (72%) belong to this class and generated the highest resolution map (Figs. S1, S2 and S3; map3; 2.9 Å nominal resolution).

To obtain the best possible consensus cryo-EM map of the entire complex, we generated a series of cryo-EM maps by focused refinement around sub-domains of the $nsp13_1$-RTC (map2) and $nsp13_2$-RTC (map3) maps and combined these, generating a composite map with a nominal resolution of 2.8 Å (Fig. 1; Figs. S1-S3, map9). Local resolution analysis [29] suggested that the active site and NiRAN ligand-binding pocket of the RdRp were resolved to between 2.1-2.6 Å resolution (Fig. S3). This was supported by the excellent quality of the cryo-EM map, where the ADP-Mg^{2+} bound in the NiRAN domain enzymatic site could be visualized (Fig. S4), and RNA base pairs near the RdRp active site could be identified directly from the cryo-EM density (Fig. S4). Although not as well resolved, the ADP-AlF_3-Mg^{2+} and surrounding residues in the nsp13 active sites could also be modeled (Fig. S4).

Despite the excellent map quality for most of the RTC (Figs. 1 and S4), features of the composite consensus map (map9) suggested substantial heterogeneity in the nsp13 subunits, particularly in the RecA2 and 1B domains (Fig. S3). Therefore, we generated a mask surrounding the nsp13.1 and nsp13.2 RecA1, RecA2, and 1B domains (of map3; Figs. 2 and S2) and used masked classification with signal subtraction [30] to identify four distinct conformational states (Figs. 2, S1, S2, and S5; Table S3) with significant differences in the dispositions of the nsp13 subunits, particularly nsp13.1.

The class II structure (Figs. 2 and S5) contains the most particles and the nsp13 subunits are best resolved in this map (map12; Figs. 2, S2 and S5). Compared to the other structures, the nsp13.1 RecA domains of class II (map12) are closed onto each other more than the other structures (Fig. S5) and are thereby engaged most tightly with the RNA (see below). We call this the 'nsp13.1-engaged' structure and use it as a reference to give a general overview of the conformational changes in the other classes.

While each of the classes shows significant changes in both the disposition of each nsp13 subunit as a whole as well as intramolecular domain motions within each nsp13 subunit, each structural class can be characterized by one dominant conformational change in nsp13.1 (compared to the nsp13.1-engaged structure used as a reference):

i) In class I, the nsp13.1 RecA2 domain is rotated open by 21° with respect to RecA1. Concomitantly, the RNA binding site is empty while occupancy of the nsp13.1 nucleotide-binding site is ambiguous. We therefore call this the 'nsp13.1-apo' structure (Fig. 2).

ii) In class III, the nsp13.1 subunit swivels as a whole by 38° away from nsp13.2. We call this the 'nsp13.1-swiveled' structure (Fig. 2).

iii) In class IV, the nsp13.1 domain 1B is rotated 85° away from the nsp13.1 RNA binding channel, creating the '1B-open' structure (Fig. 2).

The nsp13.1-engaged conformation grasps the downstream RNA t-strand

In the nsp13.1-engaged structure, the distance between the center-of-gravity of the two nsp13.1 RecA domains, 27.3 Å, is the shortest of the eight nsp13 conformations (Fig. S5). The RecA domains are thus 'closed' and grasp the downstream t-RNA single-stranded 5'-segment emerging from the RdRp active site, giving rise to well-resolved cryo-EM density for the RNA passing through the helicase (Fig. 3A). The RNA is corralled in a tunnel between the two RecA domains and the 1B domain, which is also in a closed conformation (Figs. 2 and 3A). The pattern of purine and pyrimidines in the cryo-EM density is clearly discernable, allowing the unique sequence register of the RNA engaged with the nsp13.1 helicase to be determined (Fig. 3A).

The ordered RNA segment is 7 nucleotides in length (+9 to +15; Fig. 3), with the five central nucleotides (+10 to +14) completely enclosed within the helicase. The RNA phosphate backbone generally faces the nsp13.1 RecA domains, and the mostly stacked bases face the 1B domain (Fig. 3). As might be expected, the helicase establishes extensive interactions with the RNA phosphate backbone, including several

polar interactions. Interactions with the RNA bases are mostly van der Waals interactions and not expected to be base-specific (Fig. 3).

The nsp13.1-apo state

Comparison of the nsp13.1-apo and nsp13.1-engaged structures revealed a striking change in the conformation of the RecA-like ATPase domains of nsp13.1. Superimposition of the α-carbons of nsp13.1 RecA1 (residues 235-439) or RecA2 (residues 440-596) alone yielded root-mean-square-deviations (rmsds) of 0.387 and 0.673 Å, respectively, indicating the structures of the individual domains are very similar between the two states. However, superimposition via the α-carbons of only RecA1 gave an rmsd of 7.05 Å for the RecA2 α-carbons, indicating a substantial change in the relative disposition of the two domains. The movement of RecA2 with respect to RecA1 corresponds to an ~21° rotation about the axis shown in Fig. 4A (also see Video S1), corresponding to an opening of the RecA domains; the nsp13.1 RecA domains of the nsp13.1-apo state are the furthest open of any of the eight nsp13 protomer structures (Fig. S5F).

The consensus $nsp13_2$-RTC cryo-EM map (map3; Figs. S1 and S2) contains low-resolution density indicating that the downstream single-stranded 5'-segment of the t-RNA occupies the nsp13.1 RNA binding channel (Fig. 1B). Moreover, the t-RNA 5'-segment occupying the nsp13.1 RNA binding channel of the nsp13.1-engaged state is well resolved (Fig. 3). By contrast, the nsp13.1-apo cryo-EM density shows that the nsp13.1 RNA-binding path is empty (Fig. 4B). The nsp13.1-apo cryo-EM density also does not support occupancy of ADP-AlF_3-Mg^{2+} in the nucleotide-binding site of nsp13.1, although the low resolution of the map in this region makes this conclusion tentative.

Spontaneous and reversible transition of the nsp13.1 RecA domains between the nsp13.1-engaged and nsp13.1-apo conformations

To characterize the RecA1-RecA2 interdomain movement and how a bound substrate may influence that movement, we performed MD simulations of free nsp13.1 (i.e., without nsp13.2 or the RTC) under four different substrate-bound conditions ($ATPMg^{2+}$/RNA, $ADPMg^{2+}$/RNA, $ATPMg^{2+}$ only, and $ADPMg^{2+}$ only). For each condition, we ran three independent 5-μs simulations, all initiated from the nsp13.1-engaged conformation (Figs. 2 and 3).

In simulations of $ATPMg^{2+}$/RNA-bound nsp13.1, the RecA2 domain maintained its general orientation with respect to RecA1 throughout the simulations (Fig. 4C). The average rmsd of RecA2 between the initial nsp13.1-engaged cryo-EM structure and the structures from the MD trajectories, aligned on the RecA1, was low (~2.9 Å; some adjustment of RecA2 from the initial nsp13.1-engaged cryo-EM structure position in these simulations was expected, as the cryo-EM structure was determined using ADP-AlF_3/RNA in place of $ATPMg^{2+}$/RNA). Conformations resembling the nsp13.1-apo structure (rmsd <3.5 Å) were not observed (Fig. 4C, D).

In simulations of $ADPMg^{2+}$/RNA-bound nsp13.1, RecA2 rotated away from its initial position in the nsp13.1-engaged conformation, and nsp13.1-apo–like conformations were repeatedly visited throughout the simulations (Figs .4C, D). The $ADPMg^{2+}$/RNA-bound nsp13.1-apo-like conformations were metastable, and interconverted with the nsp13.1-engaged conformations. Spontaneous and reversible conversion between the nsp13.1-engaged and nsp13.1-apo conformations was also observed in the simulations of $ATPMg^{2+}$-bound and $ADPMg^{2+}$-bound nsp13.1 (Figs. 4C, D). These results suggest that the presence of both the $ATPMg^{2+}$ and RNA may stabilize the nsp13.1-engaged conformation and that the absence of either substrate may destabilize the nsp13.1-engaged conformation and facilitate the transition to the nsp13.1-apo conformation, consistent with the observations from the cryo-EM analysis.

The '1B-open' conformation of nsp13.1 may explain how the RdRp can synthesize RNA in the presence of nsp13

In the nsp13.1-engaged state, the downstream single-stranded t-RNA is guided through a deep groove between the RecA1 and RecA2 domains that is completely closed off by the 1B domain (Fig. 5A). Remarkably, in the 1B-open structure, the nsp13.1 1B domain rotates 85° about the stalk away from the nsp13.1 RNA binding channel, creating an open groove rather than a closed tunnel (Fig. 5B). The cryo-EM density allows modeling of the downstream single-stranded t-RNA emerging from the RdRp active site up to the edge of the open groove proximal to the RdRp, but the RNA density disappears there, indicating that the RNA is not engaged within the active site of the helicase (Fig. 5B).

In the 1B-open conformation, the nsp13.1 1B domain appears to be trapped open by the presence of nsp13.2 (Fig. 5B), with the transition from the 1B-open to the 1B-closed conformation blocked by nsp13.2. Consistent with this, we analyzed the nsp13 conformational states in the $nsp13_1$-RTC (nsp13.2 absent) by masked classification with signal subtraction around the RecA1, RecA2 and 1B domains of the single nsp13 (Fig. S1) but the 1B-open nsp13 conformation was not observed. We propose that the 1B-open conformation of the nsp13.1 1B domain is trapped by the presence of nsp13.2.

We note that in the $(nsp13_2\text{-RTC})_2$ dimer (Figs. S1-S3), the nsp13 protomers corresponding to nsp13.1 are also in the '1B-open' state, as was observed by Yan *et al.* [31]. Since the dimer only comprises 8% of our particle dataset (Table S1) while the $nsp13_2$-RTC complex comprises 72% of the particles, we have focused our attention on the latter complex. We observe that the $(nsp13_2\text{-RTC})_2$ dimer forms in the absence of additional factors such as nsp10-14 [20], in contrast to what's reported in Yan *et al.* [31].

Yan *et al.* [31] observed the 1B-open state of nsp13.1 (labeled nsp13-2 in their nomenclature) in their (dimer) dCap(0)-RTC structure, curiously assigned as a backtracking-competent state. This is at odds with: i) observations that nsp13.1 in the 1B-open conformation does not engage RNA in its RNA-binding groove [Fig. 5B; also observed by Yan *et el.* [31]] and so would be incompetent for RNA translocation, and ii) the finding that nsp13 stimulated SARS-CoV-2 RTC backtracking [26].

Spontaneous transition of the nsp13.1 1B domain from the 1B-open to 1B-closed conformations

The conformations of the nsp13.1 1B domain in the nsp13.1-engaged and nsp13.1-apo structures are related by a ~10° rotation around the nsp13-stalk, but the 1B domains are closed on the nsp13-RecA domains in both structures. We refer to these collectively as '1B-closed' states (Fig. 2). These conformations have also been observed in crystal structures of isolated nsp13 as well as some other SF1-like helicases [32]. The conformation of the 1B domain in the 1B-open cryo-EM structure, in which the domain is rotated ~85° compared to the 1B-closed conformations, was only seen in nsp13.1 when it was paired with nsp13.2 in the RTC, suggesting that this conformation may not be stable in isolated nsp13. To test this hypothesis, we performed five independent 25-μs simulations on isolated (free) nsp13 (with $ADPMg^{2+}$), initiated from the 1B-open conformation (Fig. 2).

In three out of the five simulations, the 1B domain underwent a ~90° rotation from the starting 1B-open conformation around the stalk toward the RNA-binding groove to a 1B-closed conformation (Fig. 6A). These ~90° rotated 1B domain conformations closely resemble the disposition of the 1B domain in the nsp13.1-apo structure. The 1B domain rmsd between the simulation-generated structures from the last 2 μs of the three trajectories and the 1B domain in the nsp13.1-apo cryo-EM structure (aligned on the RecA1 domain) was, on average, ~3.6 Å. We also observed that a small portion (<5%) of these 1B-closed structures were more similar to the 1B domain of the nsp13.1-engaged conformation (rmsd <3.5 Å). These nsp13.1-engaged-like 1B conformations were short-lived, and once visited they quickly transitioned to the nsp13.1-apo conformation, presumably because the nsp13.1-engaged conformation was captured in the presence of RNA, which was not included in our simulations.

We next asked whether or not the 1B domain in a 1B-closed state may spontaneously transition to the 1B-open state. In each of the three simulations in which we observed a transition of the 1B domain from the 1B-open to a 1B-closed conformation, the 1B domain remained in the 1B-closed conformation through the end of the 25-μs simulation; a 1B-closed-to-open transition was not observed. We performed an additional five independent 25-μs simulations of the isolated (free) nsp13.1, initiated from the 1B-closed conformation (of the nsp13.1-engaged structure). We did not observe any transition events to the 1B-open conformation over the aggregated 125 μs simulation time. Instead, the 1B domain maintained its 1B-closed orientation in the initial structure, with some minor wobbling back and forth between the 1B-closed conformations of the nsp13.1-engaged and nsp13.1-apo structures (Fig. 6B).

Aligning the nsp13.1 simulation structures in the 1B-open-to-closed transition pathways with the nsp13.1 of the 1B-open cryo-EM structure showed that, on average, ~40% (53%, 22%, and 45% in the three simulations) of these 1B domain intermediate conformations clashed with nsp13.2, suggesting that the 1B-open-to-closed transition might be blocked by nsp13.2 (Fig. S6). Here we envisage that 1B domain transitions are facilitated by entry into the ‘swiveled’ state. The swiveled structure is characterized by one dominant conformational change; compared to the nsp13.1-engaged structure, the

nsp13.1 protomer as a whole swivels with respect to the rest of the RTC by 38°, repositioning nsp13.1 with respect to nsp13.2 (Fig. 6C).

There are some clashes between nsp13.1 and nsp13.2 when the simulation-generated structures are aligned to the swiveled cryo-EM structure, but to a much lesser extent (9%, 0%, and 2% in the three simulations; Fig. S6). This observation is consistent with the notion that the swiveled structure may be an intermediate state that facilitates the transition between the 1B-open and 1B-closed conformations.

In summary, our simulations suggest that the conformation of the 1B domain in the 1B-open structure may only be transiently stable on its own, transitioning spontaneously into the 1B-closed conformations of the nsp13.1-apo and nsp13.1-engaged structures. Such transitions may be blocked by the presence of nsp13.2 in the 1B-open $nsp13_2$-RTC. We did not observe transitions from the 1B-closed conformations to the 1B-open conformation, and we speculate that in the presence of RNA in the nsp13.1 RNA-binding groove (Fig. 3), nsp13.1 may be further stabilized in the closed 1B domain conformation.

Nsp13 conformations in $nsp13_2$-backtracked complexes

In the nsp13.1-engaged state (Fig. 2), the RdRp translocates in the 3'->5' direction on the t-RNA while nsp13.1 grasps the single-stranded t-RNA ahead of the RdRp (Fig. 3) and translocates in the 5'->3' direction (Fig. 1B). We proposed that events at the RdRp active site that would delay or stall p-RNA chain elongation (such as misincorporation or incorporation of nucleotide analogs) could allow the nsp13.1 translocation activity to push the RdRp backward on the t-RNA [20]. In this process, termed backtracking, the complex moves in the 5'->3' direction on the t-RNA accompanied by reverse-threading of the p-RNA through the complex, generating a single-stranded p-RNA 3'-fragment. In support of this hypothesis, structural and functional studies showed that the SARS-CoV-2 RdRp can backtrack, that the resulting single-stranded p-RNA 3'-fragment extrudes out the RdRp NTP-entry tunnel, and that backtracking is stimulated by nsp13 [26].

To compare the conformational states of the nsp13 protomers in the $nsp13_2$-BTCs (backtracked complexes) with the $nsp13_2$-RTCs, we used the same masked classification with signal subtraction protocol (Fig. S2) to classify the $nsp13_2$-BTC particles into four conformational states (Fig. S7). Structural models were built and rigid-body refined into the cryo-EM densities for each class except for $nsp13_2$-BTC-class2 (13% of the particles), which had very poor cryo-EM density for nsp13.1. To compare these structural models with the $nsp13_2$-RTC structures, we aligned the models for each $nsp13_2$-BTC model with the nsp13.1-engaged state by superimposing α-carbons of nsp12, yielding rmsds < 0.213 Å. We then calculated rmsds for α-carbons of nsp13.1 and nsp13.2. Both $nsp13_2$-BTC-class1 and $nsp13_2$-BTC-class4 aligned well with the nsp13.1-engaged $nsp13_2$-RTC state (Table S4) and both also had strong density for the downstream t-RNA engaged with nsp13.1 (Fig. S7). Therefore, we classify both of these structures as nsp13.1-engaged-BTCs. The $nsp13_2$-BTC-class3 structure had an open 1B domain of nsp13.1 and clearly aligned with the 1B-open-RTC structure (Table S4). Thus, in contrast to the $nsp13_2$-RTC structures, which were equally divided between the nsp13.1-engaged and 1B-open states (33% each), the $nsp13_2$-BTC structures were

heavily skewed towards the nsp13.1-engaged state (72%) vs. the 1B-open state (15%; Fig. S7).

Discussion

In this work, we observed distinct conformational states of the nsp13 protomers within the SARS-CoV-2 nsp13$_2$-RTC, providing functional insights into nsp13 and its complex with the RTC (see Video S2). Like other helicases, nsp13 is a molecular motor that translocates along single-stranded nucleic acid, unwinding structural elements in its path (Mickolajczyk et al., 2020). This process is driven by conformational changes within nsp13 resulting from NTP hydrolysis.

The conformational transition from the nsp13.1-engaged to the nsp13.1-apo structures, observed both by our cryo-EM (Fig. 4A) and MD (Figs. 4C, D) analyses, corresponds to an ~21° rotation of the RecA2 domain with respect to RecA1, opening the gap between the two domains (Fig. 4A; Video S1). The nsp13.1-engaged structure is engaged with the substrate RNA and is trapped in an 'on-pathway' conformation of the nucleotide hydrolysis cycle by the non-hydrolyzable ATP analog ADP-AlF$_3$. While the nsp13.1-apo structure, being devoid of RNA, is not 'on-pathway' *per se*, the 21° opening of the RecA2 domain from the nsp13.1-engaged to nsp13.1-apo conformations matches the disposition of the RecA2 domains in other SF1 helicases, such as human Upf1, a structural homolog of nsp13 [13,23]. The disposition of the RecA domains of Upf1 with ADP-AlF$_3$ and RNA substrate [PDB 2XZO] [33] matches the nsp13.1-engaged structure. On the other hand, the RecA domains in a structure of Upf1 with ADP (so likely on-pathway) are opened by a 24° rotation about the same axis as the 21° opening of the nsp13.1-apo RecA domains [PDB 2GK6] [34]. We thus infer that the nsp13.1-apo conformation reports on an on-pathway conformation of the RecA domains, such as in the ADP-Mg^{2+}/RNA-bound state of the translocation cycle (Figs. 4C, D). Due to the opening of the nsp13.1 RecA domains, the center-of-gravity of RecA2 shifts roughly parallel with the RNA backbone by 3.4 Å, corresponding to the rise between stacked RNA bases. This observation is suggestive of an 'inchworm' model for translocation (Video S1), as proposed for related SF1 helicase translocation on single-stranded nucleic acids [14,17,35–39].

Prior structural analysis of the nsp13$_2$-RTC identified that the nsp13.1 helicase and the RdRp translocate on the t-RNA with opposing polarities (Chen et al., 2020). In circumstances where RdRp elongation of the p-RNA is hindered (such as in the event of a misincorporation at the p-RNA 3'-end), nsp13.1 translocation activity could backtrack the RdRp [20], as shown by follow-up structural and biochemical analyses [26]. The opposing polarities of the RdRp and nsp13 translocation activities (Fig. 1B) presented a conundrum that was not addressed by these previous studies; how is it possible for the RdRp to rapidly and efficiently synthesize RNA if it is constantly being opposed by nsp13? Moreover, the predominant complex present in the nsp13-RTC samples is the nsp13$_2$-RTC complex (Table S1), but only nsp13.1 was seen to engage with the t-RNA; what is the role of nsp13.2, the second copy of nsp13 in the nsp13$_2$-RTC? The work herein suggests answers to both questions.

Maximum likelihood classification approaches revealed four distinct conformations of the nsp13 protomers in the nsp13$_2$-RTC (Figs. 2, 7; Videos S1, S2). The nsp13.1-engaged state resolves nsp13.1 clamped onto the single-stranded downstream t-RNA, providing an atomic view of nsp13 engaged with the single-stranded RNA (Fig. 3). The single-stranded t-RNA threads through a tunnel formed by a deep groove between the RecA1 and RecA2 domains and further enclosed by the 1B domain (Fig. 5A).

By contrast, the 1B-open state shows nsp13.1 adopting a conformation in which the 1B domain is rotated open ~85° about the stalk domain, leaving an open RNA binding groove (Fig. 5B). In this state, the single-stranded downstream t-RNA does not engage with the helicase. Thus, this represents an inactive state of the helicase that would be unable to translocate on the RNA.

Our structural analysis combined with MD simulations confirmed that the conformation of the nsp13.1 1B domain in the 1B-open structure is not stable on its own but is sterically trapped by the presence of nsp13.2, which blocks the conformational change required for 1B domain closure (Fig. 6A). These results suggest that the 1B-open state represents a rapidly elongating state of the nsp13$_2$-RTC, where the downstream single-stranded template RNA feeds into the RdRp active site without engaging with nsp13.1. Nsp13.2 may trap the 1B-open (inactive) state of nsp13.1, allowing RdRp elongation to proceed without opposition from the nsp13.1 helicase (Fig. 7). Finally, swiveling of nsp13.1 in the swiveled state allows space for the 1B-open to 1B-closed transition (Fig. 6C), suggesting that the swiveled state represents a transition state between the open and closed states of the 1B domain (Fig. 7). We note that the presence of nsp13.2 in the nsp13.1-engaged state would also block the 1B-closed to 1B-open transition, suggesting how nsp13.2 can enhance the helicase activity of nsp13.1 [21]

Thus, our results suggest a mechanism for the nsp13$_2$-RTC to turn backtracking on and off; switching between rapid RNA synthesis (1B-open state; elongating RdRp; Fig. 7) and backtracking (nsp13.1-engaged, backtracking RdRp; Fig. 7). In our analysis of the conformational states of the nsp13$_2$-RTC, the particles were equally divided between the nsp13.1-engaged (backtracking on) and 1B-open (backtracking off) states (Figs. S2, S7). Remarkably, an identical analysis of the backtracked nsp13$_2$-BTC [26] revealed a strikingly different distribution of particles in which the nsp13.1-engaged (backtracking on) state was heavily favored (Fig. S7). This raises the possibility that the conformational switch that turns backtracking on and off is allosterically controlled.

In MD simulations exploring the dynamics of the p-RNA 3'-nucleotide of a pre-translocated RTC, a mismatched p-RNA 3'-nucleotide frayed from the t-RNA towards and into the NTP-entry tunnel (which also serves as the backtracking tunnel; Video S1), while a p-RNA 3'-nucleotide engaged in a Watson-Crick base pair with the t-RNA did not [26]. We thus suggest that misincorporation by the RdRp leads to fraying of the p-RNA 3'-nucleotide into the NTP-entry tunnel, which may allosterically signal the rapidly elongating 1B-open state to switch to the backtracking nsp13.1-engaged state (Fig. 7). This facilitates a possible proofreading mechanism since backtracking would extrude the mismatched p-RNA 3'-nucleotide out of the NTP-entry tunnel (Fig. 7) [26], allowing the nsp10/nsp14 3'-exonuclease proofreading activity to access and degrade the

mismatched p-RNA 3'-nucleotide [40–42]. The nsp14-mediated proofreading activity is crucial for the virus to avoid mutation catastrophe while replicating its ~30 kb genome [41], and is also an important determinant of SARS-CoV-2 susceptibility to many anti-viral nucleotide analogs [43].

Acknowledgments. We thank M. Ebrahim and L. Urnavicius at The Rockefeller University Evelyn Gruss Lipper Cryo-electron Microscopy Resource Center and H. Kuang at the New York Structural Biology Center (NYSBC) for help with cryo-EM data collection, and R. Landick, T. Appleby, and members of the Darst/Campbell laboratory for helpful discussions, and M. Grasso, P.M.M. Shelton, T. M. Kapoor, P.D.B. Olinares, and B.T. Chait (The Rockefeller University) for helpful discussions and initial sample characterizations and analyses. Some of the work reported here was conducted at the Simons Electron Microscopy Center (SEMC) and the National Resource for Automated Molecular Microscopy (NRAMM) and National Center for CryoEM Access and Training (NCCAT) located at the NYSBC, supported by grants from the NIH National Institute of General Medical Sciences (P41 GM103310), NYSTAR, the Simons Foundation (SF349247), the NIH Common Fund Transformative High Resolution Cryo-Electron Microscopy program (U24 GM129539) and NY State Assembly Majority. This work was supported by the Pels Family Center for Biochemistry and Structural Biology (The Rockefeller University), and NIH grants R01 GM114450 (E.A.C.), R35 GM118130 (S.A.D.), and R01 AI161278 (E.A.C./S.A.D).

Author contributions. Conceptualization; J.C., Q.W., B.M., J.P., E.A.C., D.E.S., S.A.D.; Cloning, protein purification, biochemistry; J.C., B. M., E.L.; Cryo-EM specimen preparation; J.C., B.M., E.L.; Cryo-EM data collection and processing: J.C., K.M., E.T.E.; Model building and structural analysis: J.C., B.M., E.A.C., S.A.D.; Molecular dynamics simulation and analysis; Q.W., Y.P.; Funding acquisition and supervision: E.A.C., D.E.S., S.A.D.' Manuscript first draft: Q.W., B.M., J.P., E.A.C., D.E.S., S.A.D.; All authors contributed to finalizing the written manuscript.

Competing interests. The authors declare there are no competing interests.

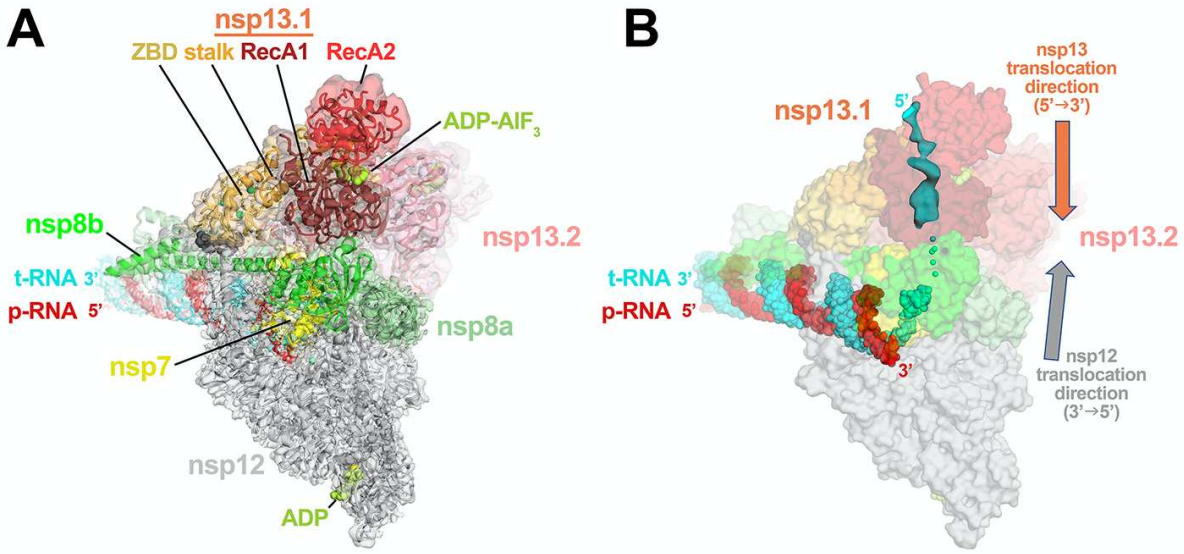

Chen et al., Figure 1

Fig. 1 | Consensus cryo-EM structure of an nsp13$_2$-RTC.

A. Overall architecture of the consensus nsp13$_2$-RTC. Shown is the transparent cryo-EM density (map3, local-resolution filtered) with the nsp13$_2$-RTC model superimposed.

B. The consensus nsp13$_2$-RTC structure is shown; RNA is shown as atomic spheres, proteins are shown as transparent molecular surfaces. A low-pass filtered (6 Å) cryo-EM difference density reveals the path of the downstream t-RNA 5'-segment through the RNA binding groove of nsp13.1 (cyan surface).

See also Figs. S1-S4.

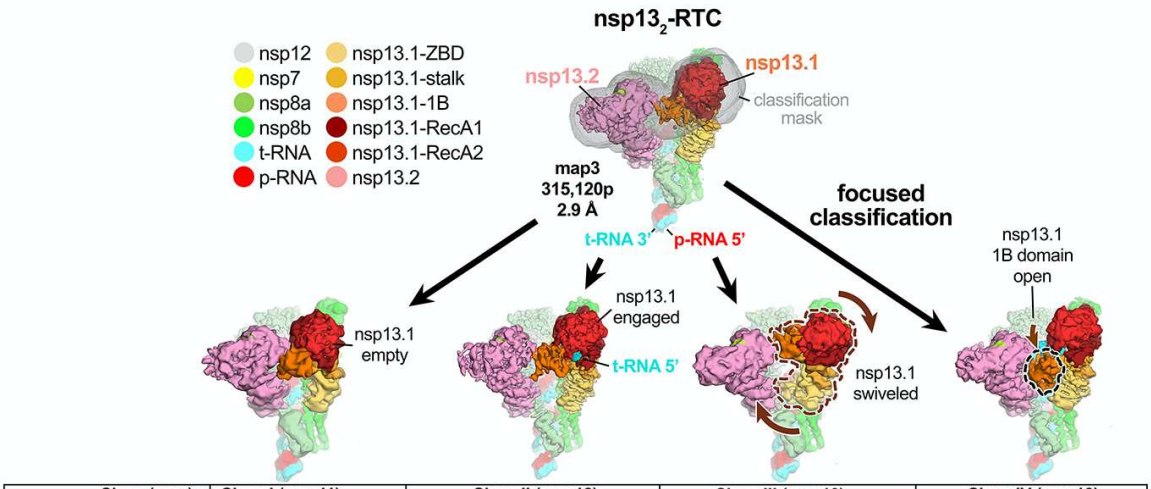

Class (map):	Class I (map11)	Class II (map12)	Class III (map10)	Class IV (map13)
Name:	Nsp13.1-apo	Nsp13.1-engaged	swiveled	1B-open
Particle # (%):	52,403p (17%)	105,272p (33%)	54,830p (17%)	102,615p (33%)
Nominal resolution (Å):	3.6 Å	3.1 Å	3.5 Å	3.1 Å
Nsp13.1 RecA status:	RecA-open	RecA-closed	RecA-closed	RecA-closed
Nsp13.1 1B status:	1B-closed	1B-closed	1B-closed	1B-open

Chen et al., Figure 2

Fig. 2 | Four conformational states of the nsp13$_2$-RTC.

(*top*) Cryo-EM density (map3, local-resolution filtered) colored according to the code on the left. A mask was constructed surrounding the nsp13.1 and nsp13.2 1B, RecA1, and RecA2 domains (grey mesh). The 315,120 particles were divided into four distinct structures (class I, II, III, and IV) by focused classification inside the mask, followed by further refinement (Figs. S1, S5). Class II contained the most particles, and the nsp13.1 RecA domains were completely closed (Fig. S5), entrapping the 5'-t-RNA segment in a groove between the two RecA domains and the 1B domain (Fig. 3). Therefore, class II (nsp13.1-engaged) was used as a reference for comparison of the other structures. Each class was characterized by one dominant conformational change:
class I) nsp13.1-apo, the RecA domains were completely open (Fig. S5) and devoid of RNA (Fig. 4), class III) swiveled, the nsp13.1 protomer as a whole was rotated 38° as shown (Fig. 6), class IV) 1B-open, the nsp13.1 1B domain was rotated open by 85° (Fig. 5).

Also see Fig. S5 and Videos S1 and S2.

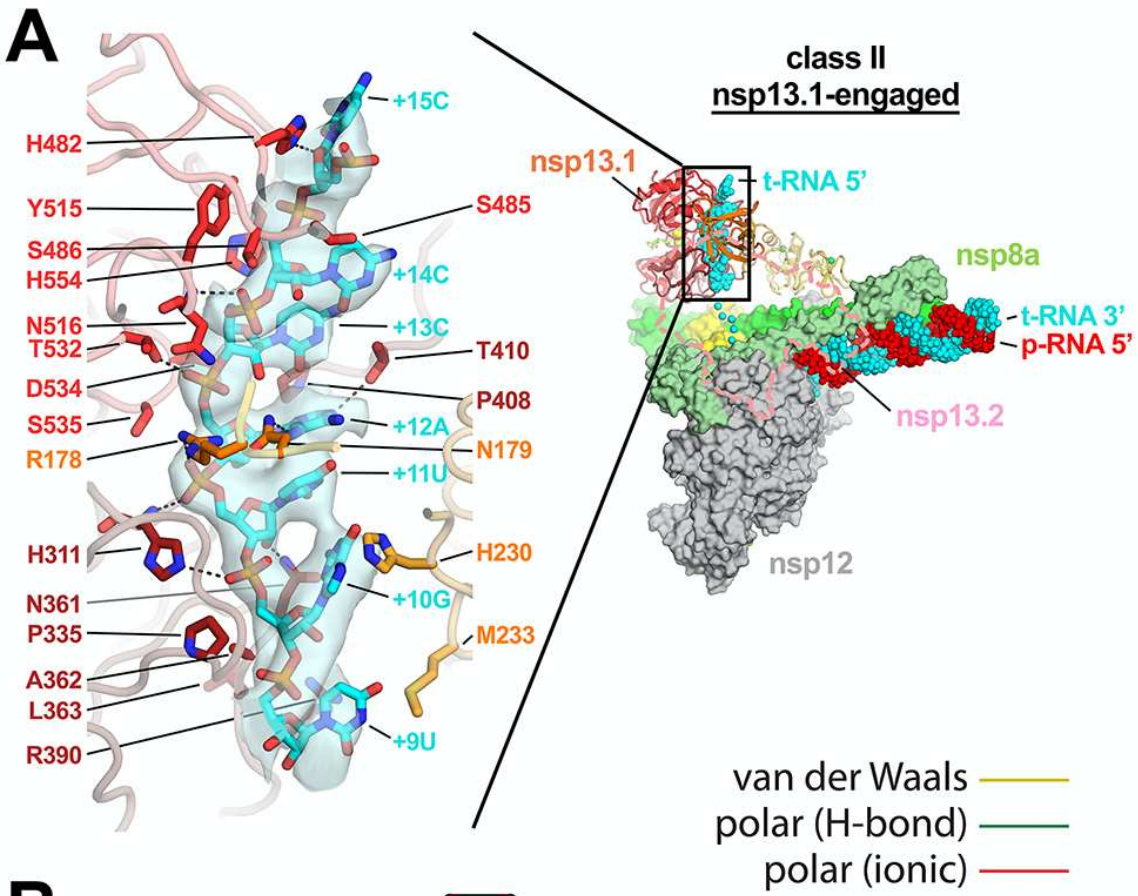

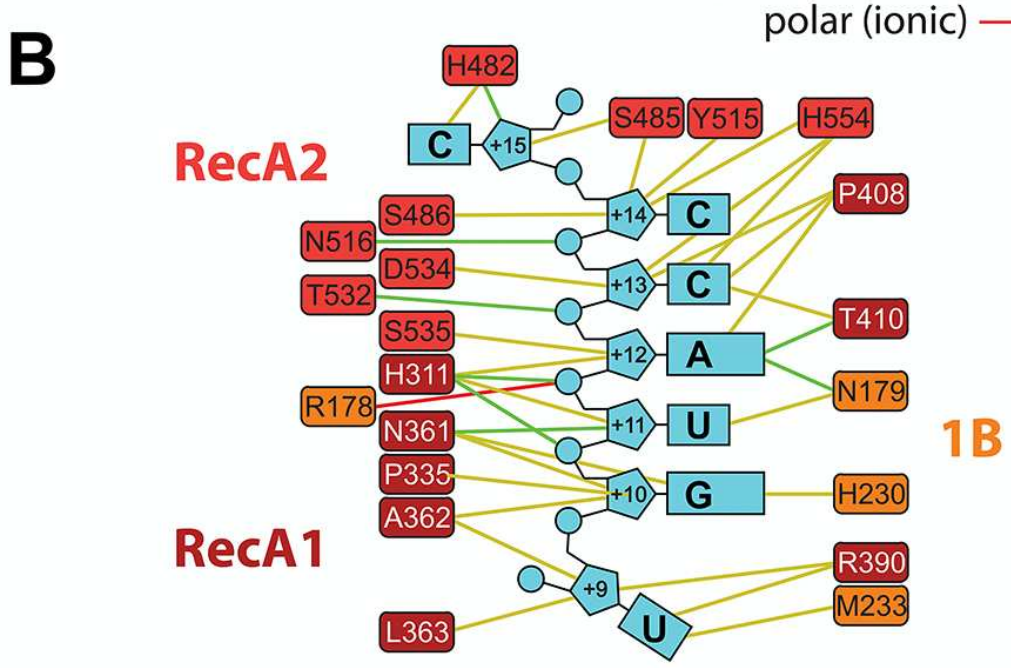

Chen et al., Figure 3

478

Fig. 3 | In class II (nsp13.1-engaged), the nsp13.1 RecA domains and 1B domain clamp onto the 5'-single-stranded t-RNA.

A. (*right*) Overall view of the nsp13.1-engaged structure. Proteins are shown as molecular surfaces except nsp13.1 is shown as a backbone ribbon, and nsp13.2 is removed and shown only as a dashed outlline. The RNA is shown as atomic spheres. The boxed region is magnified on the left.

(*left*) Nsp13.1 is shown as a backbone worm but with side chains that interact with the t-RNA shown. Cryo-EM density for the downstream 5'-t-RNA segment is shown (transparent blue surface) with the t-RNA model superimposed. The pattern of purines/pyrimidines in the RNA density was clear and unique, allowing the identification of the sequence register for the nsp13.1-bound RNA.

B. Schematic illustrating nsp13.1-RNA interactions.

Also see Video S2.

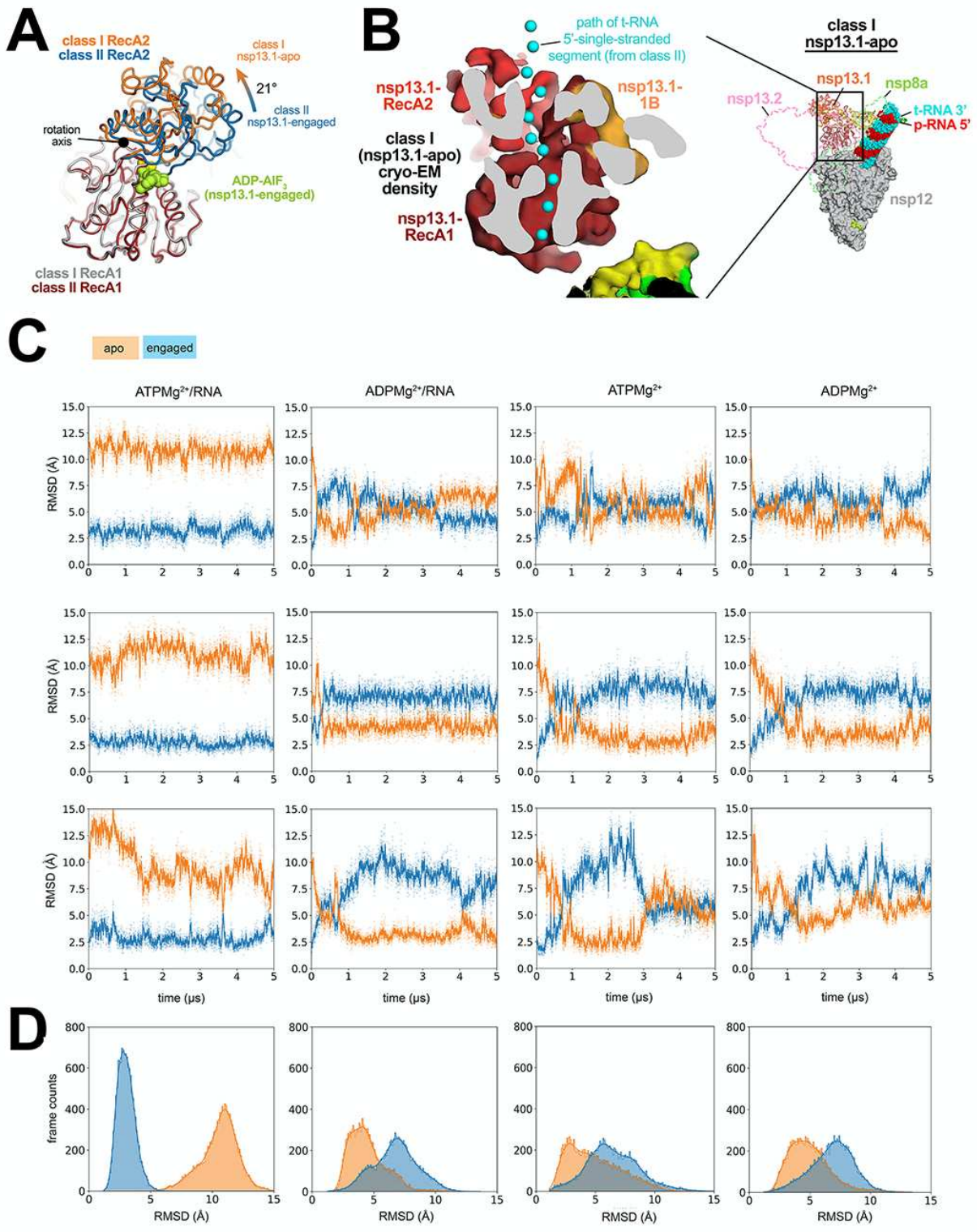

Chen et al., Figure 4

Fig. 4 | In nsp13.1-apo, the RecA domains are open and devoid of RNA density.

A. The RecA1 domains of class I (nsp13.1-apo) and class II (nsp13.1-engaged) were superimposed (rmsd of 0.387 Å over 205 α-carbons), revealing that the RecA2 domain of nsp13.1-apo was rotated open by 21° about the rotation axis shown. The ADP-AlF_3-Mg^{2+} from the nsp13.1-engaged structure is shown as limon atomic spheres.

B. (*right*) Overall view of the nsp13.1-apo structure. Proteins are shown as molecular surfaces except nsp13.1, which is shown as a backbone ribbon, and nsp13.2, which is removed and shown only as a dashed outline. The RNA is shown as atomic spheres. The boxed region is magnified on the left.

(*left*) Cryo-EM density of nsp13.1-apo reveals that the RNA path is empty (the RNA path from the nsp13.1-engaged structure is denoted by cyan spheres).

C. Three independent simulations of nsp13.1 bound to ATPMg^{2+}/RNA, ADPMg^{2+}/RNA, ATP Mg^{2+}, and ADPMg^{2+}. Values of rmsd plotted represent the heavy-atom rmsd of the RecA2 lobe (after alignment on the RecA1 lobe) with respect to nsp13.1-engaged (blue) and nsp13.1-apo (orange) cryo-EM structures.

D. The rmsd histograms represent aggregate values across all three replicates shown in (**C**).

Also see Video S1.

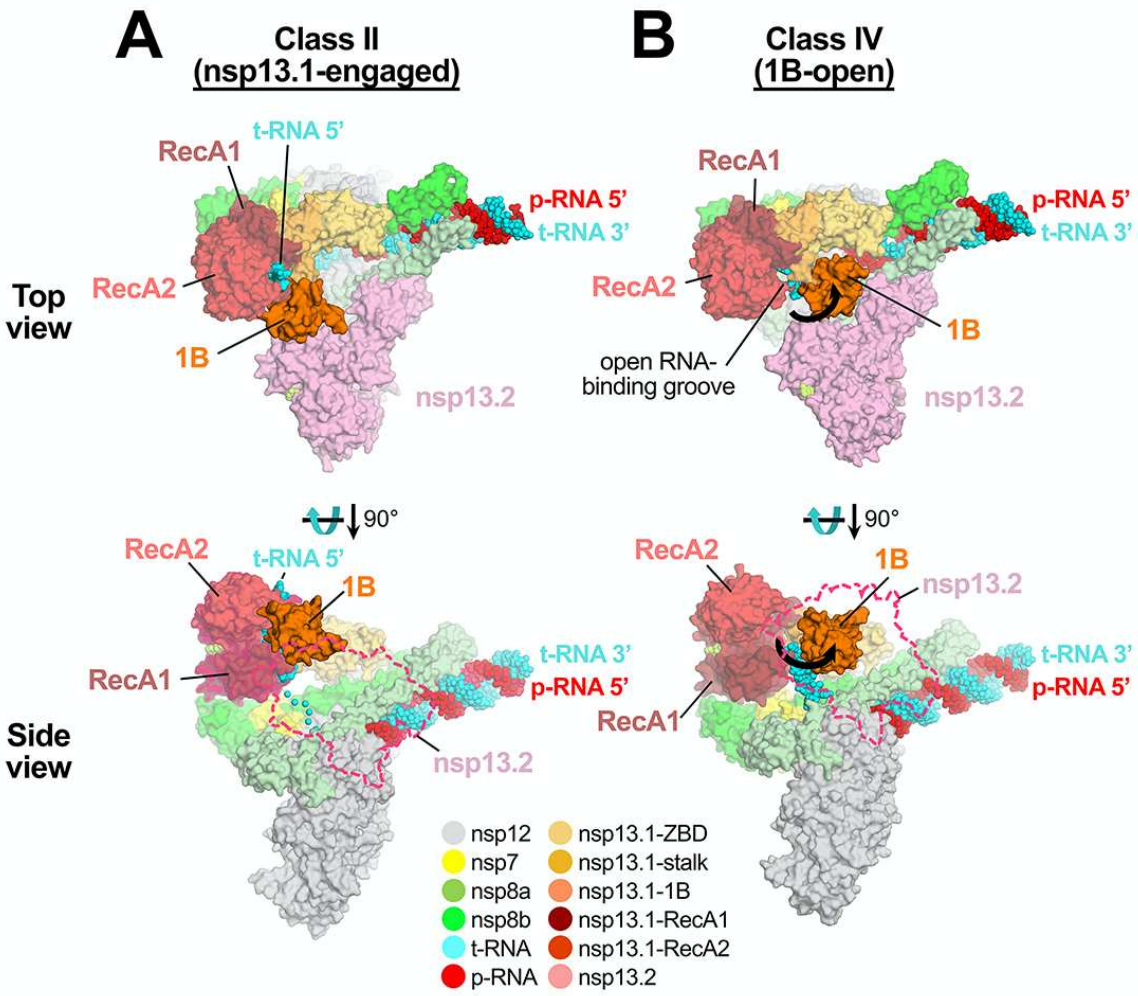

Chen et al., Figure 5

Fig. 5 | 1B-open structure.

Comparison of nsp13.1-engaged (A) and 1B-open (B) structures. Two views are shown, a top view (*top*) and a side view (*bottom*). In the top view, the proteins are shown as molecular surfaces and color-coded according to the key at the bottom. In the side view, nsp13.2 is shown only as a dashed outline. The RNA is shown as atomic spheres. In the 1B-open structure (B), the nsp13.1 1B domain is rotated open by 85° (represented by thick black arrows). The 5'-t-RNA emerging from the RdRp active site approaches the nsp13.1 RNA binding groove but does not enter it.

Also see Video S2.

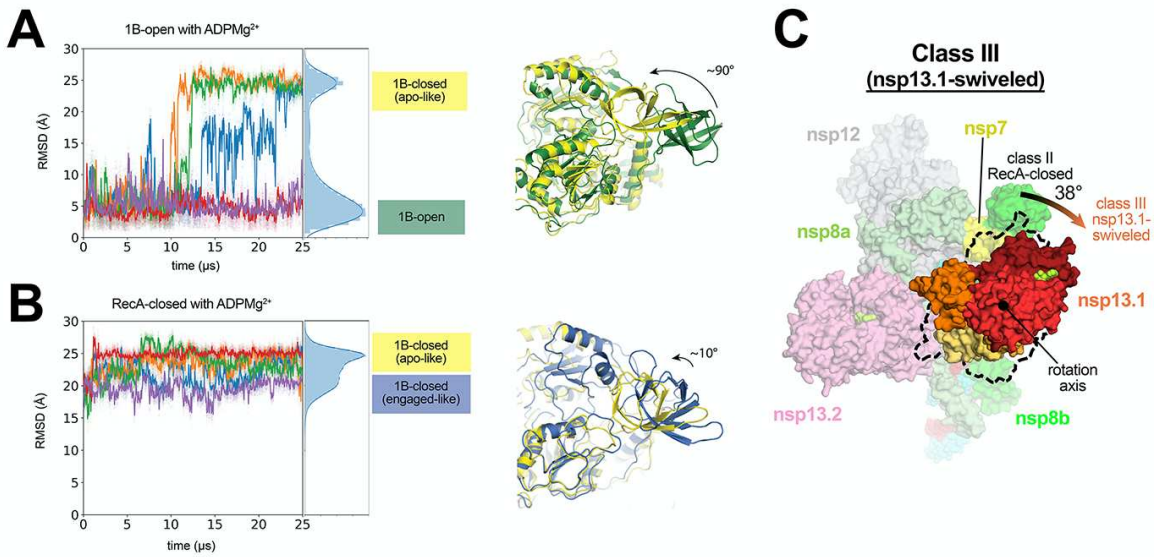

Chen et al., Figure 6

Fig. 6 | In the nsp13.1-swiveled structure, the entire nsp13.1 promoter is rotated.

A. Front view of the nsp13.1-swiveled structure, highlighting nsp13.1. The position of the nsp13.1 promoter in the nsp13.1-engaged structure is illustrated by the dashed black outline. The nsp13.1 promoter of the nsp13.1-swiveled structure is rotated by 38° as shown.

B. Five independent simulations of $ADPMg^{2+}$-bound nsp13.1, starting from the 1B-open cryo-EM structure. Values plotted represent the heavy-atom rmsd of the 1B domain (nsp13 residues 150-228) compared to the 1B domain in the 1B-open cryo-EM structure (aligned on the RecA1 domain). The rmsd histograms on the right represent aggregate values across all five simulations. Representative structures of the two major conformations from the rmsd histogram from simulations are shown (right).

C. Five independent simulations of $ADPMg^{2+}$-bound nsp13.1, starting from the nsp13.1-engaged state. Values plotted represent the heavy-atom rmsd of the 1B domain compared to the 1B domain in the 1B-open cryo-EM state (aligned on the RecA1 domain). The rmsd histograms on the far right represent aggregate values across all five simulations. Representative structures of the two major conformations from the rmsd histogram from simulations are shown (right).

See also Fig. S6.

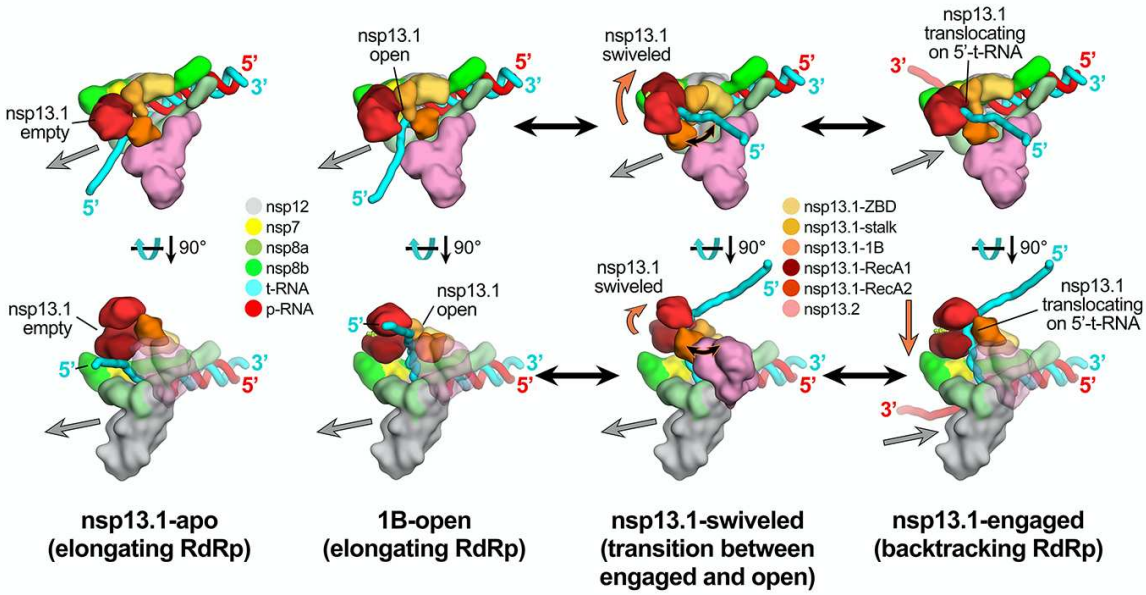

Chen et al., Figure 7

Fig. 7. Schematic model for RTC elongation (1B-open) vs. backtracking (nsp13.1-engaged) states.

Top views (top row) and side views (bottom row) of each structural class.

Nsp13.1-apo (17%): The nsp13.1 RecA domains are open, consistent with the absence of nucleotide. The nsp13.1 is therefore not engaged with the downstream 5'-t-RNA and the RdRp can freely translocate on the t-RNA with concurrent elongation of the p-RNA (gray arrow pointing downstream).

1B-open (33%): The nsp13.1 1B domain is rotated open and sterically trapped by the presence of nsp13.2. The nsp13.1 is therefore unable to engage with the downstream 5'-t-RNA and is inactive. The RdRp is able to elongate freely in the downstream direction.

Nsp13.1-swiveled (17%): The rotation of the nsp13.1 protomer away from nsp13.2 provides space for the nsp13.1 1B domain to open and/or close. We therefore propose that nsp13.1-swiveled represents a transition state between the 1B-open (elongating) and nsp13.1-engaged (backtracking) states.

Nsp13.1-engaged (33%): The nsp13.1 1B and RecA domains are clamped onto the downstream 5'-t-RNA. In this state, nsp13.1 can translocate on the t-RNA in the 5'-3' direction (shown by the orange arrow). This counteracts RdRp elongation and causes backtracking (backward motion of the RdRp on the RNA, shown by the gray arrow pointing upstream).

Also see Fig. S7 and Videos S1 and S2.

METHODS

No statistical methods were used to predetermine sample size. The experiments were not randomized, and the investigators were not blinded to allocation during experiments and outcome assessment.

Protein expression and purification

SARS-CoV-2 nsp12 was expressed and purified as described [20]. Briefly, a pRSFDuet-1 plasmid containing His_6-SUMO SARS-CoV-2 nsp12 (Addgene #159107) was transformed into *E. coli* BL21-CodonPlus cells (Agilent). Cells were grown and protein expression was induced by the addition of isopropyl β-d-1-thiogalactopyranoside (IPTG). Cells were collected and lysed in a French press (Avestin). The lysate was cleared by centrifugation and purified on a HiTrap Heparin HP column (Cytiva). The fractions containing nsp12 were loaded onto a HisTrap HP column (Cytiva) for further purification. Eluted nsp12 was dialyzed, cleaved with His_6-Ulp1 SUMO protease, and passed through a HisTrap HP column to remove the SUMO protease. Flow-through was collected, concentrated by centrifugal filtration (Amicon), and loaded on a Superdex 200 Hiload 16/600 (Cytiva). Glycerol was added to the purified nsp12, aliquoted, flash-frozen with liquid N_2, and stored at -80°C.

SARS-CoV-2 nsp7/8 was expressed and purified as described [20]. Briefly, the pCDFDuet-1 plasmid containing His_6 SARS-CoV-2 nsp7/8 (Addgene #159092) was transformed into *E. coli* BL21 (DE3). Cells were grown and protein expression was induced by the addition of IPTG. Cells were collected and lysed in a French press (Avestin). The lysate was cleared by centrifugation and purified on a HisTrap HP column (Cytiva). Eluted nsp7/8 was dialyzed, cleaved with His_6-Prescission Protease to cleave His_6 tag, and then passed through a HisTrap HP column to remove the protease (Cytiva). Flow-through was collected, concentrated by centrifugal filtration (Amicon), and loaded onto a Superdex 75 Hiload 16/600 (Cytiva). Glycerol was added to the purified nsp7/8, aliquoted, flash-frozen with liquid N_2, and stored at -80°C.

SARS-CoV-2 nsp13 was expressed and purified as described [20]. Briefly, the pet28 plasmid containing His_6 SARS-CoV-2 nsp13 (Addgene #159390) was transformed into *E. coli* Rosetta (DE3) (Novagen). Cells were grown and protein expression was induced by the addition of IPTG. Cells were collected and lysed in a French press (Avestin). The lysate was cleared by centrifugation and purified on a HisTrap HP column (Cytiva). Eluted nsp13 was dialyzed, cleaved with His_6-Prescission Protease, and then passed through a HisTrap HP column to remove protease (Cytiva). Flow-through was collected, concentrated by centrifugal filtration (Amicon), and loaded onto a Superdex 200 Hiload 16/600 (Cytiva). Glycerol was added to the purified nsp13, aliquoted, flash-frozen with liquid N_2, and stored at -80°C.

Preparation of SARS-CoV-2 nsp13-replication/transcription complex (RTC) for Cryo-EM. Cryo-EM samples of SARS-CoV-2 nsp13-RTC were prepared as described [20]. Briefly, purified nsp12 and nsp7/8 were concentrated, mixed in a 1:3 molar ratio, and incubated for 20 min at 22ºC. Annealed RNA scaffold (Horizon Discovery, Ltd.) was

added to the nsp7/8/12 mixture and incubated for 15 min at 22°C. Sample was buffer exchanged into cryo-EM buffer [20 mM HEPES pH 8.0, 150 mM K-Acetate,10 mM $MgCl_2$, 2 mM DTT] and further incubated for 20 min at 30°C. The sample was purified over a Superose 6 Increase 10/300 GL column (Cyriva) in cryo-EM buffer. The peak corresponding to nsp7/8/12/RNA complex was pooled and concentrated by centrifugal filtration (Amicon). Purified nsp13 was concentrated by centrifugal filtration (Amicon) and buffer exchanged into cryo-EM buffer. Buffer exchanged nsp13 was mixed with ADP (1 mM final) and AlF_3 (1 mM final) and then added to nsp7/8/12/RNA at a molar ratio of 1:1. Complex was then incubated for 5 min at 30°C.

Cryo-EM grid preparation. Prior to grid freezing, 3-([3-cholamidopropyl]dimethylammonio)-2-hydroxy-1-propanesulfonate (CHAPSO, Anatrace) was added to the sample (8 mM final), resulting in a final complex concentration of 8 µM. The final buffer condition for the cryo-EM sample was 20 mM HEPES pH 8.0, 150 mM K-Acetate,10 mM $MgCl_2$, 2 mM DTT, 1 mM ADP, 1 mM AlF_3, 8 mM CHAPSO. C-flat holey carbon grids (CF-1.2/1.3-4Au, EMS) were glow-discharged for 20 s prior to the application of 3.5 µL of sample. Using a Vitrobot Mark IV (Thermo Fisher Scientific), grids were blotted and plunge-froze into liquid ethane with 90% chamber humidity at 4°C.

Cryo-EM data acquisition and processing. Structural biology software was accessed through the SBGrid consortium [44]. Grids were imaged using a 300 kV Titan Krios (Thermo Fisher Scientific) equipped with a GIF BioQuantum and K3 camera (Gatan). Images were recorded with Leginon [45] with a pixel size of 1.07 Å/px (micrograph dimension of 5760 × 4092 px) over a defocus range of −0.8 µm to −2.5 µm with a 20 eV slit. Movies were recorded in "counting mode" (native K3 camera binning 2) with ~30 e-/px/s in dose-fractionation mode with subframes of 50 ms over a 2.5 s exposure (50 frames) to give a total dose of ~66 e-/$Å^2$. Dose-fractionated movies were gain-normalized, drift-corrected, summed, and dose-weighted using MotionCor2 [46]. The contrast transfer function (CTF) was estimated for each summed image using the Patch CTF module in cryoSPARC v2.15.0 [47]. Particles were picked and extracted from the dose-weighted images with box size of 256 px using cryoSPARC Blob Picker and Particle Extraction. The entire dataset consisted of 17,806 motion-corrected images with 3,750,107 particles. Particles were sorted using two rounds of cryoSPARC 2D classification (N=100, where N equals the number of classes), resulting in 661,105 curated particles that were re-extracted with a boxsize of 320 px. An initial model was generated using cryoSPARC *Ab initio* Reconstruction (N=3) on a subset of the particles. Particles were further curated using this initial model as a 3D template for cryoSPARC Heterogeneous Refinement (N=3), resulting in 451,760 particles (green map, Fig. S1). Curated particles were further classified using cryoSPARC Heterogeneous Refinement (N=3). Each of the resulting 3D classes were further processed with cryoSPARC *Ab initio* Reconstruction (N=3), generating three distinct models that could be used to sort particles [Ref 1: $nsp13_1$-RTC, Ref 2: $nsp13_2$-RTC, Ref 3: $(nsp13_2\text{-RTC})_2$]. Using Ref 1-3 as 3D templates for Heterogeneous Refinement (N=6), multi-reference classification was performed on the 451,760 curated particles. Classification revealed

three unique classes: nsp13$_1$-RTC (class1; 85,206 particles; yellow), nsp13$_2$-RTC (class2-4; 315,216 particles; red), and (nsp13$_2$-RTC)$_2$ (class5; 35,403 particles; blue). Particles within each class were further processed using RELION 3.1-beta Bayesian Polishing [48]. Polished particles were refined using cryoSAPRC Local and Global CTF Refinement in combination with cryoSPARC Non-uniform Refinement [49], resulting in structures with the following particle counts and nominal resolutions: nsp13$_1$-RTC (85,187 particles; 3.2 Å), nsp13$_2$-RTC (315,120 particles; 2.9 Å), (nsp13$_2$-RTC)$_2$ (35,392 particles; 3.3 Å). To facilitate model building of nsp13$_2$-RTC, particles from nsp13$_1$-RTC and nsp13$_2$-RTC were combined in a cryoSPARC Non-uniform Refinement, subtracted (masking the RTC), and further refined with cryoSPARC Local Refinement using a mask encompassing the RTC. The resulting map, deemed RTC (local), had nominal resolution of 2.8 Å. Additionally, particles from the nsp13$_2$-RTC were subtracted in different regions (using separate masks for nsp12-NiRAN, nsp13.1, and nsp13.2) and the particles from each subtraction were further refined with masked cryoSPARC Local Refinement. The resulting maps had the following nominal resolutions: nsp13.1(local): 3.4 Å, nsp13.2(local): 3.3 Å, nsp12-NiRAN(local): 2.7 Å. Locally refined maps were combined into an nsp13$_2$-RTC composite map using PHENIX 'Combine Focused Maps' [50,51], with resulting nominal resolution of 2.8 Å. The nsp13-RecA domains in particles from the nsp13$_1$-RTC and nsp13$_2$-RTC classes were sorted using particle subtraction (masking around the RecA domains, shown as red mesh in Fig. S1), followed by masked RELION 3D classification. Classification of RecA domains in the nsp13$_1$-RTC particles (pale yellow) did not reveal discrete conformational heterogeneity in the RecA domains. However, classification of RecA domains in the nsp13$_2$-RTC particles (light red) revealed unique conformations of the RecA domains with the following particle counts and nominal resolutions: RecA classI (52,403 particles; 3.5 Å), RecA class II (102,615 particles; 3.1 Å), RecA class III (54,830 particles; 3.5 Å), RecA class IV (105,272 particles; 3.1 Å). Local resolution calculations were generated using blocres and blocfilt from the Bsoft package [29].

Model building and refinement. For an initial model of the nsp13$_2$-RTC, the initial RTC model was derived from PDB 6XEZ [20] and the initial nsp13 model from PDB 6ZSL [32]. The models were manually fit into the cryo-EM density maps using Chimera [52] and rigid-body and real-space refined using Phenix real-space-refine [50,51]. For real-space refinement, rigid body refinement was followed by all-atom and B-factor refinement with Ramachandran and secondary structure restraints. Models were inspected and modified in Coot [53].

Molecular dynamics simulations

General simulation setup and parameterization. Proteins, ATP, ADP, and ions were parameterized with the DES-Amber SF1.0 force field [54]. RNAs were parameterized with the Amber ff14 RNA force field [55] with modified electrostatic, van der Waals, and torsional parameters to more accurately reproduce the energetics of nucleobase stacking [56]. The systems were solvated with water parameterized with the TIP4P-D water model [57] and neutralized with a 150 mM NaCl buffer. The systems each contained ~160,000 atoms in a 110 × 110 × 110 Å cubic box.

Systems were first equilibrated on GPU Desmond using a mixed NVT/NPT schedule [58], followed by a 1 μs relaxation simulation on Anton, a special-purpose machine for molecular dynamics simulations [59]. All production simulations were performed on Anton and initiated from the last frame of the relaxation simulation. Production simulations were performed in the NPT ensemble [60] at 310 K using the Martyna-Tobias-Klein barostat [61]. The simulation time step was 2.5 fs, and a modified r-RESPA integrator [62] was used in which long-range electrostatic interactions were evaluated every three time steps. Electrostatic forces were calculated using the *u*-series method [63]. A 9-Å cutoff was applied for the van der Waals calculations.

System preparation. The initial conformations of Class II nsp13.1 bound to the various substrates ($ATPMg^{2+}$/RNA, $ADPMg^{2+}$/RNA, $ATPMg^{2+}$, and $ADPMg^{2+}$) were prepared based on the cryo-EM structure of the Class II $nsp13_2$-BTC_5. The initial conformation of the Class IV, 1B-open nsp13.1 structure was prepared from the cryo-EM Class IV $nsp13_2$-BTC_5 structure. AlF_3 was removed from the active site. Missing loops and termini in proteins were capped with ACE/NME capping groups. In simulations with ATP at the active site, ATP was manually placed using ADP in the cryo-EM structure as the reference. The systems were prepared for simulation using the Protein Preparation Wizard in Schrödinger Maestro (Schrödinger Release 2020-4: Maestro, Schrödinger, LLC, New York, NY, 2020).

Simulation analysis. The average rmsd was calculated for the RecA2 domain (residues 450–690) and 1B domain (residues 145–200) of nsp13.1 between the cryo-EM structures and instantaneous structures from the trajectories, aligned on the RecA1 lobe (residues 240–440). Simulation structures shown in figures were rendered using PyMol (The PyMOL Molecular Graphics System, Version 2.0 Schrödinger, LLC).

Quantification and statistical analysis. The local resolution of the cryo-EM maps (Figs S3 and S5) was estimated using blocres [29] with the following parameters: box size 15, sampling 1.1, and cutoff 0.5. Directional 3DFSCs (Figs. S3 and S5) were calculated using 3DFSC [64]. The quantification and statistical analyses for model refinement and validation were generated using MolProbity [65] and PHENIX [51].

Data and code availability. All unique/stable reagents generated in this study are available without restriction from one of the Lead Contacts, Seth A. Darst (darst@rockefeller.edu). The cryo-EM density maps and atomic coordinates have been deposited in the EMDataBank and Protein Data Bank as follows: $nsp13_1$-RTC (EMD-24431, 7RE2), $nsp13_2$-RTC (composite) (EMD-24430, 7RE1), $(nsp13_2\text{-RTC})_2$ (EMD-24432, 7RE3), $nsp13_2$-RTC (nsp13.1-apo) (EMD-24428, 7RDZ), $nsp13_2$-RTC (nsp13.1-engaged) (EMD-24427, 7RDY), $nsp13_2$-RTC (nsp13.1-swiveled) (EMD-24429, 7RE0), $nsp13_2$-RTC (1B-open) (EMD-24426, 7RDX). The MD trajectories described in this work are available at https://www.deshawresearch.com/downloads/download_trajectory_sarscov2.cgi/.

745 **REFERENCES**
746

747 1. Wu, F. *et al.* A new coronavirus associated with human respiratory disease in China.
748 *Nature* 579, 265–269 (2020).

749 2. Zhou, P. *et al.* A pneumonia outbreak associated with a new coronavirus of probable
750 bat origin. *Nature* 579, 270–273 (2020).

751 3. Subissi, L. *et al.* One severe acute respiratory syndrome coronavirus protein complex
752 integrates processive RNA polymerase and exonuclease activities. *Proceedings of the*
753 *National Academy of Sciences of the United States of America* 111, E3900-9 (2014).

754 4. Kirchdoerfer, R. N. & Ward, A. B. Structure of the SARS-CoV nsp12 polymerase
755 bound to nsp7 and nsp8 co-factors. *Nature Communications* 10, 2342–9 (2019).

756 5. Hillen, H. S. *et al.* Structure of replicating SARS-CoV-2 polymerase. *Nature* 1–6
757 (2020) doi:10.1038/s41586-020-2368-8.

758 6. Gordon, C. J. *et al.* Remdesivir is a direct-acting antiviral that inhibits RNA-dependent
759 RNA polymerase from severe acute respiratory syndrome coronavirus 2 with high
760 potency. *J Biol Chem* 295, 6785–6797 (2020).

761 7. Tchesnokov, E. P. *et al.* Template-dependent inhibition of coronavirus RNA-
762 dependent RNA polymerase by remdesivir reveals a second mechanism of action. *J*
763 *Biol Chem* 295, 16156–16165 (2020).

764 8. Kokic, G. *et al.* Mechanism of SARS-CoV-2 polymerase stalling by remdesivir. *Nat*
765 *Commun* 12, 279 (2021).

766 9. Snijder, E. J., Decroly, E. & Ziebuhr, J. The Nonstructural Proteins Directing
767 Coronavirus RNA Synthesis and Processing. *Adv Virus Res* 96, 59–126 (2016).

768 10. Dinten, L. C. van, Tol, H. van, Gorbalenya, A. E. & Snijder, E. J. The Predicted
769 Metal-Binding Region of the Arterivirus Helicase Protein Is Involved in Subgenomic
770 mRNA Synthesis, Genome Replication, and Virion Biogenesis. *J Virol* 74, 5213–5223
771 (2000).

772 11. Seybert, A., Dinten, L. C. van, Snijder, E. J. & Ziebuhr, J. Biochemical
773 Characterization of the Equine Arteritis Virus Helicase Suggests a Close Functional
774 Relationship between Arterivirus and Coronavirus Helicases. *J Virol* 74, 9586–9593
775 (2000).

776 12. Seybert, A. *et al.* A Complex Zinc Finger Controls the Enzymatic Activities of
777 Nidovirus Helicases. *J Virol* 79, 696–704 (2005).

778 13. Lehmann, K. C., Snijder, E. J., Posthuma, C. C. & Gorbalenya, A. E. What we know
779 but do not understand about nidovirus helicases. *Virus Res* 202, 12–32 (2015).

780 14. Saikrishnan, K., Powell, B., Cook, N. J., Webb, M. R. & Wigley, D. B. Mechanistic
781 basis of 5'-3' translocation in SF1B helicases. *Cell* 137, 849–59 (2009).

782 15. Adedeji, A. O. *et al.* Mechanism of Nucleic Acid Unwinding by SARS-CoV Helicase.
783 *Plos One* 7, e36521 (2012).

784 16. Mickolajczyk, K. J. *et al.* Force-dependent stimulation of RNA unwinding by SARS-
785 CoV-2 nsp13 helicase. *Biophys J* (2020) doi:10.1016/j.bpj.2020.11.2276.

786 17. Singleton, M. R., Dillingham, M. S. & Wigley, D. B. Structure and Mechanism of
787 Helicases and Nucleic Acid Translocases. *Annu Rev Biochem* 76, 23–50 (2007).

788 18. Hao, W. *et al.* Crystal structure of Middle East respiratory syndrome coronavirus
789 helicase. *Plos Pathog* 13, e1006474 (2017).

790 19. Jia, Z. *et al.* Delicate structural coordination of the Severe Acute Respiratory
791 Syndrome coronavirus Nsp13 upon ATP hydrolysis. *Nucleic Acids Res* 47, 6538–6550
792 (2019).

793 20. Chen, J. *et al.* Structural basis for helicase-polymerase coupling in the SARS-CoV-2
794 replication-transcription complex. *Cell* 182, 1560-1573.e13 (2020).

795 21. Yan, L. *et al.* Architecture of a SARS-CoV-2 mini replication and transcription
796 complex. *Nat Commun* 11, 5874 (2020).

797 22. Yan, L. *et al.* Cryo-EM Structure of an Extended SARS-CoV-2 Replication and
798 Transcription Complex Reveals an Intermediate State in Cap Synthesis. *Cell* 184, 184-
799 193.e10 (2021).

800 23. Deng, Z. *et al.* Structural basis for the regulatory function of a complex zinc-binding
801 domain in a replicative arterivirus helicase resembling a nonsense-mediated mRNA
802 decay helicase. *Nucleic Acids Res* 42, 3464–77 (2013).

803 24. Tavares, R. de C. A., Mahadeshwar, G., Wan, H., Huston, N. C. & Pyle, A. M. The
804 Global and Local Distribution of RNA Structure throughout the SARS-CoV-2 Genome. *J*
805 *Virol* 95, (2021).

806 25. Huston, N. C. *et al.* Comprehensive in vivo secondary structure of the SARS-CoV-2
807 genome reveals novel regulatory motifs and mechanisms. *Mol Cell* 81, 584-598.e5
808 (2021).

809 26. Malone, B. *et al.* Structural basis for backtracking by the SARS-CoV-2 replication–
810 transcription complex. *Proc National Acad Sci* 118, e2102516118 (2021).

27. Seifert, M. *et al.* Signatures and mechanisms of efficacious therapeutic ribonucleotides against SARS-CoV-2 revealed by analysis of its replicase using magnetic tweezers. *Biorxiv* 2020.08.06.240325 (2020) doi:10.1101/2020.08.06.240325.

28. Scheres, S. H. W. RELION: implementation of a Bayesian approach to cryo-EM structure determination. *Journal of structural biology* 180, 519–530 (2012).

29. Cardone, G., Heymann, J. B. & Steven, A. C. One number does not fit all: mapping local variations in resolution in cryo-EM reconstructions. *Journal of structural biology* 184, 226–236 (2013).

30. Bai, X., Rajendra, E., Yang, G., Shi, Y. & Scheres, S. H. W. Sampling the conformational space of the catalytic subunit of human γ-secretase. *eLife* 4, e11182 (2015).

31. Yan, L. *et al.* Coupling of N7-methyltransferase and 3′-5′ exoribonuclease with SARS-CoV-2 polymerase reveals mechanisms for capping and proofreading. *Cell* 184, 3474-3485.e11 (2021).

32. Newman, J. A. *et al.* Structure, Mechanism and Crystallographic fragment screening of the SARS-CoV-2 NSP13 helicase. *Biorxiv* 2021.03.15.435326 (2021) doi:10.1101/2021.03.15.435326.

33. Chakrabarti, S. *et al.* Molecular mechanisms for the RNA-dependent ATPase activity of Upf1 and its regulation by Upf2. *Mol Cell* 41, 693–703 (2011).

34. Cheng, Z., Muhlrad, D., Lim, M. K., Parker, R. & Song, H. Structural and functional insights into the human Upf1 helicase core. *Embo J* 26, 253–264 (2007).

35. Dillingham, M. S., Wigley, D. B. & Webb, M. R. Demonstration of Unidirectional Single-Stranded DNA Translocation by PcrA Helicase: Measurement of Step Size and Translocation Speed †. *Biochemistry-us* 39, 205–212 (2000).

36. Lohman, T. M., Tomko, E. J. & Wu, C. G. Non-hexameric DNA helicases and translocases: mechanisms and regulation. *Nat Rev Mol Cell Bio* 9, 391–401 (2008).

37. Tomko, E. J., Fischer, C. J., Niedziela-Majka, A. & Lohman, T. M. A Nonuniform Stepping Mechanism for E. coli UvrD Monomer Translocation along Single-Stranded DNA. *Mol Cell* 26, 335–347 (2007).

38. Velankar, S. S., Soultanas, P., Dillingham, M. S., Subramanya, H. S. & Wigley, D. B. Crystal structures of complexes of PcrA DNA helicase with a DNA substrate indicate an inchworm mechanism. *Cell* 97, 75–84 (1999).

39. Yarranton, G. T. & Gefter, M. L. Enzyme-catalyzed DNA unwinding: Studies on Escherichia coli rep protein. *Proc National Acad Sci* 76, 1658–1662 (1979).

845 40. Minskaia, E. *et al.* Discovery of an RNA virus 3'->5' exoribonuclease that is critically
846 involved in coronavirus RNA synthesis. *Proc National Acad Sci* 103, 5108–5113 (2006).

847 41. Gorbalenya, A. E., Enjuanes, L., Ziebuhr, J. & Snijder, E. J. Nidovirales: Evolving
848 the largest RNA virus genome. *Virus Res* 117, 17–37 (2006).

849 42. Denison, M. R., Graham, R. L., Donaldson, E. F., Eckerle, L. D. & Baric, R. S.
850 Coronaviruses: An RNA proofreading machine regulates replication fidelity and
851 diversity. *Rna Biol* 8, 270–279 (2011).

852 43. Agostini, M. L. *et al.* Coronavirus Susceptibility to the Antiviral Remdesivir (GS-
853 5734) Is Mediated by the Viral Polymerase and the Proofreading Exoribonuclease. *Mbio*
854 9, e00221-18 (2018).

855 44. Morin, A. *et al.* Collaboration gets the most out of software. *eLife* 2, e01456 (2013).

856 45. Suloway, C. *et al.* Automated molecular microscopy: the new Leginon system.
857 *Journal of structural biology* 151, 41–60 (2005).

858 46. Zheng, S. Q. *et al.* MotionCor2: anisotropic correction of beam-induced motion for
859 improved cryo-electron microscopy. *Nature methods* 14, 331–332 (2017).

860 47. Punjani, A., Rubinstein, J. L., Fleet, D. J. & Brubaker, M. A. cryoSPARC: algorithms
861 for rapid unsupervised cryo-EM structure determination. *Nat Methods* 14, 290–296
862 (2017).

863 48. Zivanov, J. *et al.* New tools for automated high-resolution cryo-EM structure
864 determination in RELION-3. *eLife* 7, (2018).

865 49. Punjani, A., Zhang, H. & Fleet, D. J. Non-uniform refinement: adaptive regularization
866 improves single-particle cryo-EM reconstruction. *Nat Methods* 17, 1214–1221 (2020).

867 50. Afonine, P. V. *et al.* New tools for the analysis and validation of cryo-EM maps and
868 atomic models. *Acta crystallographica. Section D, Structural biology* 74, 814–840
869 (2018).

870 51. Adams, P. D. *et al.* PHENIX: a comprehensive Python-based system for
871 macromolecular structure solution. *Acta Crystallographica Section D Biological*
872 *Crystallography* 66, 213–221 (2010).

873 52. Pettersen, E. F. *et al.* UCSF Chimera--a visualization system for exploratory
874 research and analysis. *Journal of computational chemistry* 25, 1605–1612 (2004).

875 53. Emsley, P. & Cowtan, K. Coot: model-building tools for molecular graphics. *Acta*
876 *Crystallographica Section D Biological Crystallography* 60, 2126–2132 (2004).

877 54. Piana, S., Robustelli, P., Tan, D., Chen, S. & Shaw, D. E. Development of a Force
878 Field for the Simulation of Single-Chain Proteins and Protein–Protein Complexes. *J*
879 *Chem Theory Comput* 16, 2494–2507 (2020).

880 55. Maier, J. A. *et al.* ff14SB: Improving the Accuracy of Protein Side Chain and
881 Backbone Parameters from ff99SB. *J Chem Theory Comput* 11, 3696–3713 (2015).

882 56. Tan, D., Piana, S., Dirks, R. M. & Shaw, D. E. RNA force field with accuracy
883 comparable to state-of-the-art protein force fields. *Proc National Acad Sci* 115,
884 201713027 (2018).

885 57. Piana, S., Donchev, A. G., Robustelli, P. & Shaw, D. E. Water Dispersion
886 Interactions Strongly Influence Simulated Structural Properties of Disordered Protein
887 States. *J Phys Chem B* 119, 5113–5123 (2015).

888 58. Bowers, K. J. *et al.* Scalable Algorithms for Molecular Dynamics Simulations on
889 Commodity Clusters. *Acm Ieee Sc 2006 Conf Sc'06* 43–43 (2006)
890 doi:10.1109/sc.2006.54.

891 59. Shaw, D. E. *et al.* Anton 2: Raising the Bar for Performance and Programmability in
892 a Special-Purpose Molecular Dynamics Supercomputer. *Sc14 Int Conf High Perform*
893 *Comput Netw Storage Analysis* 41–53 (2014) doi:10.1109/sc.2014.9.

894 60. Lippert, R. A. *et al.* Accurate and efficient integration for molecular dynamics
895 simulations at constant temperature and pressure. *J Chem Phys* 139, 164106 (2013).

896 61. Martyna, G. J., Tobias, D. J. & Klein, M. L. Constant pressure molecular dynamics
897 algorithms. *J Chem Phys* 101, 4177–4189 (1994).

898 62. Tuckerman, M., Berne, B. J. & Martyna, G. J. Reversible multiple time scale
899 molecular dynamics. *J Chem Phys* 97, 1990–2001 (1992).

900 63. Predescu, C. *et al.* The u -series: A separable decomposition for electrostatics
901 computation with improved accuracy. *J Chem Phys* 152, 084113 (2020).

902 64. Tan, Y. Z. *et al.* Addressing preferred specimen orientation in single-particle cryo-
903 EM through tilting. *Nature methods* 14, 793–796 (2017).

904 65. Chen, V. B. *et al.* MolProbity: all-atom structure validation for macromolecular
905 crystallography. *Acta Crystallographica Section D Biological Crystallography* 66, 12–21
906 (2010).

907